Quantitative comparisons of forward problems in MEEG.

Emmanuel Olivi, Maureen Clerc, Mariette Yvinec, Théodore Papadopoulo

INSTITUT NATIONAL DE RECHERCHE EN INFORMATIQUE ET EN AUTOMATIQUE

Quantitative comparisons of forward problems in MEEG.

Emmanuel Olivi, Mariette Yvinec, Maureen Clerc and Theodore Papadopoulo

N° 6364

Novembre 2008

Thème NUM

ISSN 0249-6399 ISRN INRIA/RR--6364--FR+ENG

Quantitative comparisons of forward problems in MEEG.

Emmanuel Olivi, Mariette Yvinec*, Maureen Clerc and Theodore Papadopoulo†

Thème NUM — Systèmes numériques
Équipes-Projets GEOMETRICA And ODYSSEE

Rapport de recherche n° 6364 — Novembre 2008 — 29 pages

Abstract: This document gives comparisons between several methods that solve the forward problem in MEEG by comparing their precision on a 3-layer spherical model. These methods are based on finite elements which either use surfacic meshes with triangles, volumic meshes with tetrahedra, or implicit elements deduced from levelsets.

Key-words: MEG, EEG, MEEG, forward problem, CGAL, FEM, BEM, implicit finite elements, mesh generation, Boundary element method, spherical model

* GEOMETRICA
† ODYSSEE

Centre de recherche INRIA Sophia Antipolis – Méditerranée
2004, route des Lucioles, BP 93, 06902 Sophia Antipolis Cedex (France)
Téléphone : +33 4 92 38 77 77 — Télécopie : +33 4 92 38 77 65

Comparaisons quantitatives de résultats de problèmes directs en MEEG.

Résumé : Ce document fournit des comparaisons de plusieurs méthodes de résolution du problème direct en MEEG en comparant leur précision sur un modèle de tête sphérique à trois couches. Les méthodes exposées sont des éléments finis de trois types : surfaciques (BEM), volumiques tetraèdriques (FEM), volumiques implicites basés sur des level-sets (implicit FEM).

Mots-clés : MEG, EEG, MEEG, problème direct, CGAL, éléments finis, éléments finis implicites, maillage, éléments frontière, modèle sphérique

Contents

1 Introduction

MEEG, which stands for Magneto-Electro EncephaloGraphy, is a non-invasive technique very useful in studying brain functional activity. Its high temporal resolution is order of magnitude higher than that of the functional MRI. Data acquisition in EEG and MEG gives respectively the electric potential and one component of the magnetic field on sensors located around the scalp. From these acquisitions, one can wish to recover the electrical sources inside the brain that are responsible of the electromagnetic field measured. This problem is an inverse problem of localization whose resolution requires the resolution of the forward problem. Forward problem consists in simulating sources inside the brain and computing the resulting field at the sensor positions. This resolution is done by solving Maxwell's equations in their quasi-static approximation on a geometry that depends on the patient. Hence, this problem depends on the subject, meaning that for each patient one needs the definition of the tissues, *i.e.* the geometry of the different layers and their conductivities. Most of the layers of the head can be extracted from anatomical MRI (Magnetic Resonance Imaging); the skull still present some difficulties to be extracted and is often guessed by inflating the brain. Conductivities of the layers can be evaluated by different ways ; one can use reference conductivities that have been measured in vivo on test subjects, or one can wish to estimate the conductivity for each subject using Electrical Impedance Tomography [2]. The skull conductivity is anisotropic, the tangential conductivity can be ten times higher than the radial one. It has been shown that this anisotropy has an important influence on the results of the forward (and hence inverse) problem [7]. Several methods for solving the forward problem have been proposed. Two of them require a mesh of the geometry of the specific patient's head in order to do the computations whereas the other one avoids this time and memory consuming step by doing so the computation on the grid given by the MRI. This document gives comparisons between three different methods for solving the forward problem:

- **the boundary element method (BEM),** which comes from an integral formulation of Maxwell's equations, it needs a surfacic mesh of the surfaces defining the computational domain. This method cannot take into account the anisotropy of the skull and can only handle piecewise constant conductivities.
- **the tetrahedral finite element method (tFEM),** which arises from a variational formulation of our problem, needs a volumic mesh (made of tetrahedra) of all the computational domain. It can handle anisotropy.
- **the implicit finite element method (iFEM),** which also comes from the variational formulation but uses implicit elements given by the voxels of the MRI. It can also handle anisotropy.

In order to compare the precision of these methods, we have used the very popular spherical model for which an analytical solution exists.

We first present the mesh generation using the Computational Geometry Algorithms Library (CGAL), then we explain the differences between the methods used to solve the forward problem, and we finally show the comparisons made.

2 The mesh generation

CGAL[1] is a library developed by an European consortium in which GEOMETRICA team takes part. CGAL provides an automatic mesh generation of either volumic or surfacic objects. These objects can be defined through gray-level images or equations to be satisfied.

2.1 The three-layer spherical model

The common three-layer spherical model is an idealized description of the head made of three concentric spheres with radii 0.87, 0.92, 1 that represent the cortex, the skull and the scalp of a human head (see Fig.1).

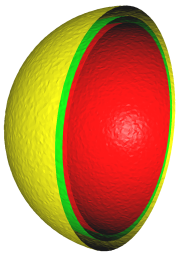

Figure 1: Surfaces describing the spherical model.

2.1.1 Volumic meshes using Head_mesher

The Head_mesher code developed from CGAL takes gray-level images and gives a volumic mesh in agreement of one or more surfaces defined by a gray level. The first step is a Delaunay refinement which adds vertices following criteria of size and shape on the mesh elements but also takes into account the distance to the surfaces to be discretized. Then, a review of all tetrahedra is performed in order to modified the slivers, which are badly shaped tetrahedra, assigning a weight to some vertices. This step is called an exudation stage. The final quantity of vertices is controlled by the choice of the maximum number of edges. This code gave us meshes with 9 000 to 600 000 vertices (see Fig.2).

[1] Computational Geometry Algorithms Library, http://www.cgal.org

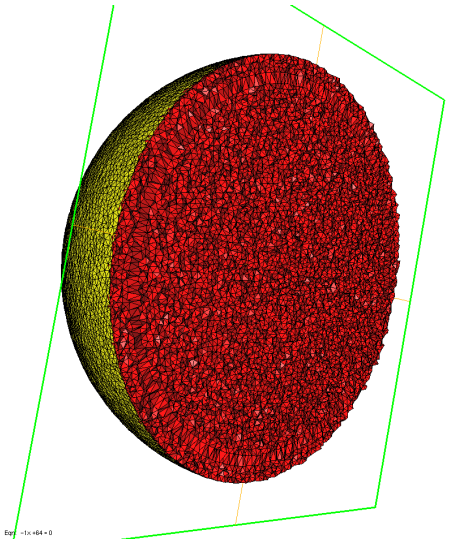

Figure 2: Volumic meshes of the sphere.

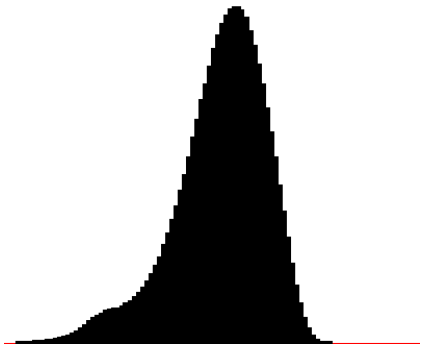

Figure 3: Dihedral angles histogram from 0 to 90°.

Figure 3 shows the histogram of the dihedral angles of the mesh generated with 310 000 vertices. This overview on the dihedral angle reflects the quality of the mesh in regards to the FEM that will be used later. We see that although minimal angles are closed to 4.7°, a high proportion of angles are enclosed between 10°and 70°.

2.1.2 Surfacic meshes using Surface_mesher

In order to run the BEM code, one needs to deal with surfacic meshes. Surfacic meshes extracted from the volumic meshes given by Head_mesher were to big to be used by the BEM. We decided to use another possibility of CGAL which is to deliver a surfacic mesh given an implicit function of the sphere:
$x^2 + y^2 + z^2 = r^2$, with $r \in \{0.87, 0.92, 1\}$. In order not to favorize the BEM whose accuracy errors may be reduced for homothetic meshes [12] we generated a different mesh for each sphere.

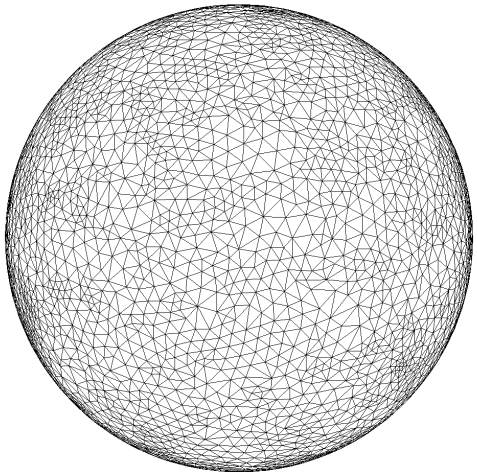

Figure 4: Surfacic mesh from an implicit function.

2.2 Realistic model

2.2.1 Volumic meshes using Head_mesher

Number of vertices	57 000	320 000	584 000
Total Time	6.62	205.34	615.46
Refining Time	0.71	7.08	17.32
Exudation Time	4.94	183.28	544.20
Validation Time	0.20	1.25	2.31
Writing Time	0.75	13.57	51.34

Table 1: Meshing steps time in minute.

The human head and its complex geometry, due to circonvolutions of the gray matter and to the closed surfaces, reveals to be a challenge for a mesher. The head model that has been used is made of four surfaces representing:

- The gray Matter (gm)
- The inner skull
- The outer skull
- The scalp

These surfaces can be very close to each other as we can see fig.6. We have succeeded to get meshes from 57 000 vertices in 6 minutes to 584 000 vertices in 10 hours. Table 1 shows that the main time consumption is due to the exudation of the slivers[2]. This time could be reduced by changing the stopping criterion in the exudation step.

[2]Computations done on a 4 processors Xeon 3.20 GHz computer with 2 MB Cache and 8GB RAM

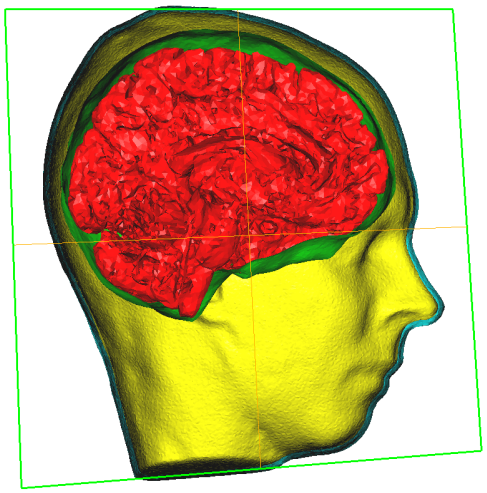

Figure 5: Describing surfaces of a realistic model.

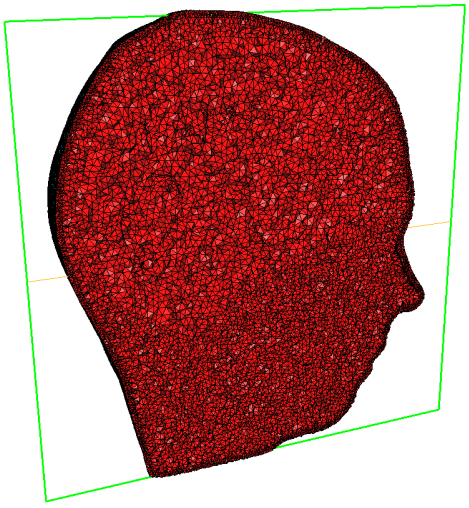

Figure 6: Volumic mesh with 584 000 vertices.

2.2.2 Surfacic meshes extracted from the volumic meshes

Surfacic mesh representing the gray matter extracted from the previous volumic mesh. This mesh contains 12 666 points.

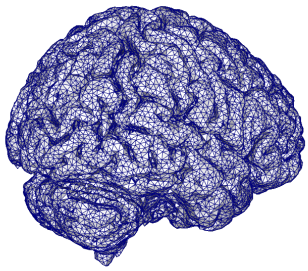

Figure 7: Surfacic mesh of the cortex.

3 Different ways of solving the forward problem in MEEG

Neuronal activity inside the cortex creates an electromagnetic field outside the head that can be measured using sensors as electrodes for the electric potential or SQUIDS (superconducting quantum magnetic sensors) for the magnetic field. From the Maxwell equations, one can obtain formulas that give the potential and the magnetic field due the parameters of a source f. In our study, we have modeled the primary current source as a current dipole $\mathbf{J}_p$ which has a discrete position r_0 and a moment $\mathbf{q}$ so that $\mathbf{J}_p = \mathbf{q}\,\delta(r_0)$. The so called forward problem, computes the resulting field on the scalp for a known source within the brain. One can derive from the quasi-static approximation of Maxwell's equations the equation for the electric potential:

$$\begin{cases} \nabla \cdot (\Sigma \nabla V) = f = \nabla \cdot \mathbf{J}_p & \text{in } \Omega \\ (\Sigma\ \nabla V) \cdot n = 0 & \text{on } \Gamma, \end{cases} \tag{1}$$

where Ω represents the conductive domain of the head and Γ its boundary. And the Biot-Savart law for the magnetic field:

$$\begin{aligned} \mathbf{B}(\mathbf{r}) = \mathbf{B}_0(\mathbf{r}) - \frac{\mu_0}{4\pi} \int_\Omega \Sigma \nabla V \times \nabla \left(\frac{1}{\|\mathbf{r} - \mathbf{r}'\|} \right) \mathrm{d}\mathbf{r}' \\ \mathbf{B}_0(\mathbf{r}) = \frac{\mu_0}{4\pi} \int_\Omega \mathbf{J}_p \times \nabla \left(\frac{1}{\|\mathbf{r} - \mathbf{r}'\|} \right) \mathrm{d}\mathbf{r}' \end{aligned} \tag{2}$$

In this document, we will present three methods to solve the forward EEG and two for the MEG forward problem.

3.1 The symmetric Boundary Element Method

3.1.1 sBEM for EEG

The boundary element method only works with piecewise constant conductivities *i.e.* constant conductivity in each volume Ω_i as shown figure 8. Let us add that the symmetric BEM can also handle non-nested volumes [6] but for sake of simplicity we will deal with the nested volume formulation. The equation 1 now becomes:

$$\begin{aligned} \sigma_i \Delta V = f \quad & \text{in } \Omega_i, \text{ for all } i = 1, \ldots, N \\ \Delta V = 0 \quad & \text{in } \Omega_{N+1} \\ \left[V\right]_j = \left[\sigma \partial_{\mathbf{n}} V\right]_j = 0 \quad & \text{on } S_j, \text{ for all } j = 1, \ldots, N \end{aligned} \tag{3}$$

The boundary element method is based on an integral formulation of the previous equations. The classical integral formulation has been derived by Geselowitz [3] and is a double-layer potential approach. This classical formulation suffers from numerical errors when applied to the E/MEG problem. A

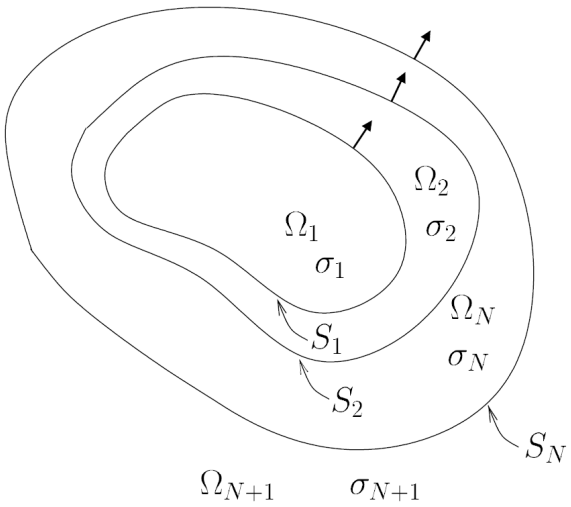

Figure 8: Nested regions with constant conductivities.

dual formulation using single-layer potential has been developed for the E/MEG problem and finally, a combination of the single and the double-layer potentials has yielded a new formulation which is symmetric and turns out to be numerically more accurate than the two others [4]. The boundary element method has the great advantage that it only requires computations on the surfaces and so does not need the entire volume to be meshed but only its describing surfaces. This reduction of dimensionality is due to the representation theorem [1, 8]. Given the Green function G solution of the following Laplace equation:

$$G(\mathbf{r}) = \frac{1}{4\pi\|\mathbf{r}\|} \qquad \text{satisfying} \qquad -\Delta G = \delta_0 \ , \tag{4}$$

and given a regular surface as boundary ($\partial\Omega$), we write down the following integral operators that will be useful to define the solution:

$$\begin{aligned}
\big(\mathcal{D}f\big)(\mathbf{r}) &= \int_{\partial\Omega} \partial_{\mathbf{n}'} G(\mathbf{r}-\mathbf{r}') f(\mathbf{r}')\,\mathrm{d}s(\mathbf{r}') \ , \\
\big(\mathcal{S}f\big)(\mathbf{r}) &= \int_{\partial\Omega} G(\mathbf{r}-\mathbf{r}') f(\mathbf{r}')\,\mathrm{d}s(\mathbf{r}') \ , \\
\big(\mathcal{N}f\big)(\mathbf{r}) &= \int_{\partial\Omega} \partial^2_{\mathbf{n},\mathbf{n}'} G(\mathbf{r}-\mathbf{r}') f(\mathbf{r}')\,\mathrm{d}s(\mathbf{r}') \ , \\
\big(\mathcal{D}^*f\big)(\mathbf{r}) &= \int_{\partial\Omega} \partial_{\mathbf{n}} G(\mathbf{r}-\mathbf{r}') f(\mathbf{r}')\,\mathrm{d}s(\mathbf{r}') \ .
\end{aligned} \tag{5}$$

Then, one can derive from these formulas a symmetric formulation, in a similar way that Nédélec [8] did. The symmetric approach, uses both the single and double-layer potentials. In this approach, we consider in each $\Omega_1, \ldots, \Omega_N$ the function:

$$u_{\Omega_i} = \begin{cases} V - v_{\Omega_i}/\sigma_i & \text{in } \Omega_i \\ -v_{\Omega_i}/\sigma_i & \text{in } \mathbb{R}^3 \backslash \overline{\Omega}_i \ . \end{cases}$$

Each u_{Ω_i} is harmonic in $\mathbb{R}^3 \backslash \partial\Omega_i$. Considering the nested volume model (Fig. 8), the boundary of Ω_i is $\partial\Omega_i = S_{i-1} \cup S_i$. With respect to the orientations of normals indicated, the jumps of u_{Ω_i} across S_i satisfy the relations:

$$[u_{\Omega_i}]_i = V_{S_i}, \qquad [u_{\Omega_i}]_{i-1} = -V_{S_{i-1}} \ , \tag{6a}$$

and the jumps of their derivatives:

$$[\partial_{\mathbf{n}} u_{\Omega_i}]_i = (\partial_{\mathbf{n}} V)^-_{S_i}, \quad [\partial_{\mathbf{n}} u_{\Omega_i}]_{i-1} = -(\partial_{\mathbf{n}} V)^+_{S_{i-1}} \ . \tag{6b}$$

We define $p_{S_i} = \sigma_i [\partial_{\mathbf{n}} u_{\Omega_i}]_i = \sigma_i (\partial_{\mathbf{n}} V)^-_{S_i}$. Note that since $[\sigma \partial_{\mathbf{n}} V] = 0$, we have $p_{S_i} = \sigma_i (\partial_{\mathbf{n}} V)^-_{S_i} = \sigma_{i+1} (\partial_{\mathbf{n}} V)^+_{S_i}$ at the interface S_i.

Applying the representation theorem to the harmonic function u_{Ω_i}, we get the following for $i = 1, \ldots, N$:

$$\begin{aligned} \sigma_{i+1}^{-1} (v_{\Omega_{i+1}})_{S_i} - \sigma_i^{-1} (v_{\Omega_i})_{S_i} = \\ \mathcal{D}_{i,i-1} V_{S_{i-1}} - 2\mathcal{D}_{ii} V_{S_i} + \mathcal{D}_{i,i+1} V_{S_{i+1}} - \sigma_i^{-1} \mathcal{S}_{i,i-1} p_{S_{i-1}} \\ + (\sigma_i^{-1} + \sigma_{i+1}^{-1}) \mathcal{S}_{ii} p_{S_i} - \sigma_{i+1}^{-1} \mathcal{S}_{i,i+1} p_{S_{i+1}} \ , \end{aligned} \tag{7}$$

Using the same approach, we evaluate the quantities $\left(\sigma_i \partial_{\mathbf{n}} u_{\Omega_i}\right)^-_{S_i} = \left(p - \partial_{\mathbf{n}} v_{\Omega_i}\right)^-_{S_i}$ and $\left(\sigma_{i+1} \partial_{\mathbf{n}} u_{\Omega_{i+1}}\right)^+_{S_i} = \left(p - \partial_{\mathbf{n}} v_{\Omega_{i+1}}\right)^+_{S_i}$ and subtracting the resulting expressions yield to:

$$\begin{aligned} (\partial_{\mathbf{n}} v_{\Omega_{i+1}})_{S_i} - (\partial_{\mathbf{n}} v_{\Omega_i})_{S_i} = \\ \sigma_i \mathcal{N}_{i,i-1} V_{S_{i-1}} - (\sigma_i + \sigma_{i+1}) \mathcal{N}_{ii} V_{S_i} + \sigma_{i+1} \mathcal{N}_{i,i+1} V_{S_{i+1}} - \\ \mathcal{D}^*_{i,i-1} p_{S_{i-1}} + 2\mathcal{D}^*_{ii} p_{S_i} - \mathcal{D}^*_{i,i+1} p_{S_{i+1}} \ , \end{aligned} \tag{8}$$

for $i = 1, \ldots, N$. Here (and in (7)) the terms corresponding to non-existing surfaces S_0, S_{N+1} are to be set to zero. Terms involving p_{S_N} must also be set to zero, since $\sigma_{N+1} = 0$ implies $p_{S_N} = 0$.

Observe that, unlike in the previous approaches, each surface only interacts with its neighbors, at the cost of considering two sets of unknowns, V_{S_i} and p_{S_i}. Equations (7) and (8) thus lead to a block-diagonal symmetric operator matrix (see fig.9). Note that the vanishing conductivity $\sigma_{N+1} = 0$ is taken into account by effectively chopping off the last line and column of the matrix.

$$
\begin{bmatrix}
\sigma_{1,2}\mathcal{N}_{11} & -2\mathcal{D}_{11}^{*} & -\sigma_2\mathcal{N}_{12} & \mathcal{D}_{12}^{*} & & & & \\
-2\mathcal{D}_{11} & \sigma_{1,2}^{-1}\mathcal{S}_{11} & \mathcal{D}_{12} & -\sigma_2^{-1}\mathcal{S}_{12} & & & & \\
-\sigma_2\mathcal{N}_{21} & \mathcal{D}_{21}^{*} & \sigma_{2,3}\mathcal{N}_{22} & -2\mathcal{D}_{22}^{*} & \dots & & & \\
\mathcal{D}_{21} & -\sigma_2^{-1}\mathcal{S}_{21} & -2\mathcal{D}_{22} & \sigma_{2,3}^{-1}\mathcal{S}_{22} & \dots & & & \\
 & & \vdots & \vdots & \ddots & & & \\
 & & & & & \sigma_{N-1,N}\mathcal{N}_{N-1,N-1} & -2\mathcal{D}_{N-1,N-1}^{*} & -\sigma_N\mathcal{N}_{N-1,N} \\
 & & & & & -2\mathcal{D}_{N-1,N-1} & \sigma_{N-1,N}^{-1}\mathcal{S}_{N-1,N-1} & \mathcal{D}_{N-1,N} \\
 & & & & & -\sigma_N\mathcal{N}_{N,N-1} & \mathcal{D}_{N,N-1}^{*} & \sigma_N\mathcal{N}_{N,N}
\end{bmatrix}
\cdot
\begin{bmatrix}
V_{S_1} \\ p_{S_1} \\ V_{S_2} \\ p_{S_2} \\ V_{S_3} \\ p_{S_3} \\ \vdots \\ V_{S_N}
\end{bmatrix}
=
\begin{bmatrix}
(\partial_{\mathbf{n}} v_{\Omega_1})_{S_1} - (\partial_{\mathbf{n}} v_{\Omega_2})_{S_1} \\
\sigma_2^{-1}(v_{\Omega_2})_{S_1} - \sigma_1^{-1}(v_{\Omega_1})_{S_1} \\
(\partial_{\mathbf{n}} v_{\Omega_2})_{S_2} - (\partial_{\mathbf{n}} v_{\Omega_3})_{S_2} \\
\sigma_3^{-1}(v_{\Omega_3})_{S_2} - \sigma_2^{-1}(v_{\Omega_2})_{S_2} \\
(\partial_{\mathbf{n}} v_{\Omega_3})_{S_3} - (\partial_{\mathbf{n}} v_{\Omega_4})_{S_3} \\
\sigma_4^{-1}(v_{\Omega_4})_{S_3} - \sigma_3^{-1}(v_{\Omega_3})_{S_3} \\
\vdots \\
(\partial_{\mathbf{n}} v_{\Omega_N})_{S_N}
\end{bmatrix}
$$

Figure 9: System representing the continuous operator version of the symmetric method. Observe that the system is symmetric and block-diagonal. Special care is needed in writing the last block because of the conductivity $\sigma_{N+1} = 0$. We have noted $\sigma_{i,i+1}$ the sum $\sigma_i + \sigma_{i+1}$ and $\sigma_{i,i+1}^{-1}$ the sum $\sigma_i^{-1} + \sigma_{i+1}^{-1}$.

3.1.2 sBEM for MEG

As one can note from equation 2, the magnetic field **B** can be fully deduced from the knowledge of V on the interfaces. With the piecewise-constant conductivity model, the ohmic term can be decomposed as a sum over volumes of constant conductivity:

$$\int \sigma \nabla V \times \frac{\mathbf{r}-\mathbf{r}'}{\|\mathbf{r}-\mathbf{r}'\|^3} d\mathbf{r}' = \sum_i \sigma_i \int_{\Omega_i} \nabla V \times \frac{\mathbf{r}-\mathbf{r}'}{\|\mathbf{r}-\mathbf{r}'\|^3} d\mathbf{r}' = \sum_i \sigma_i I_i \qquad (9)$$

In the above identity, note that the conductivities must not only be assumed constant in each domain Ω_i but, but also isotropic, in order to take σ_i out of the integral over Ω_i. The volume integral I_i can be expressed as a surface integral on $\partial\Omega_i = S_{i-1} \cup S_i$. With this in view, we use the Stokes formula, and the identity:

$$\nabla \times (V \nabla g) = \nabla V \times \nabla g$$

Thus,

$$\begin{aligned} I_i &= \int_{\Omega_i} \nabla \times \left(V(\mathbf{r}') \frac{\mathbf{r}-\mathbf{r}'}{\|\mathbf{r}-\mathbf{r}'\|^3} \right) d\mathbf{r}' = \int_{\partial\Omega_i} \mathbf{n} \times V(\mathbf{r}') \frac{\mathbf{r}-\mathbf{r}'}{\|\mathbf{r}-\mathbf{r}'\|^3} ds \\ &= \int_{S_i} \mathbf{n} \times V(\mathbf{r}') \frac{\mathbf{r}-\mathbf{r}'}{\|\mathbf{r}-\mathbf{r}'\|^3} ds - \int_{S_{i-1}} \mathbf{n} \times V(\mathbf{r}') \frac{\mathbf{r}-\mathbf{r}'}{\|\mathbf{r}-\mathbf{r}'\|^3} ds \end{aligned}$$

This expression is then inserted in 9 ans recalling, that $\sigma_{N+1} = 0$,

$$\mathbf{B}(\mathbf{r}) = \mathbf{B}_0(\mathbf{r}) + \frac{\mu_0}{4\pi} \sum_{i=1}^{N} (\sigma_i - \sigma_{i+1}) \int_{S_i} V(\mathbf{r}') \mathbf{n}' \times \nabla \left(\frac{1}{\|\mathbf{r}-\mathbf{r}'\|} \right) ds'(\mathbf{r}').$$

3.2 The tetrahedral Finite Element Method

The Finite Element Method developed for the forward problem in EEG, deals with the weak formulation of equation 1. This equation is obtain by choosing a solution in a discretized space, multiplying both sides by a test function ϕ and then integrating over the all computational domain. Using the divergence theorem we get the following equivalences:

$$\begin{aligned} \int_\Omega \nabla \cdot (\sigma \nabla V)\, \phi \, d\Omega &= \int_\Omega \nabla \cdot \mathbf{J}_p \, \phi \, d\Omega \\ \int_{\partial\Omega} (\phi\, \sigma \nabla V) \cdot \mathbf{n} \, d\partial\Omega - \int_\Omega \sigma \nabla V \cdot \nabla \phi \, d\Omega &= -\int_\Omega \mathbf{J}_p \cdot \nabla \phi \, d\Omega + \int_{\partial\Omega} \mathbf{J}_p \, \phi \cdot \mathbf{n} \, d\partial\Omega \\ \int_\Omega \sigma \nabla V \cdot \nabla \phi \, d\Omega &= \int_\Omega \mathbf{J}_p \cdot \nabla \phi \, d\Omega \end{aligned} \tag{10}$$

We then discretize our solution V decomposing its values at the nodes location using the finite basis function ϕ_i as $V = \sum_{i=1}^{n} V_i \phi_i$ on the discretized computational domain Ω_h. Using Galerkin method, which uses the same basis functions as test functions, we can decompose these integrals on each element which in the tFEM, are tetrahedra. The integrals are then performed on tetrahedra of different shapes with constant conductivity inside. The mesh is coming from our volumic mesh generator and must have several properties as discussed in the section 2.1.1. Finally, we get the matricial equation that has to be solved:

$$A\, x = b, \tag{11}$$

where x is the vector of the unknowns, the potential V_i at the grid point i — and A the matrix such that:

$$\begin{aligned} A_{i,j} &= \int_{\Omega_h} \sigma(\mathbf{r}) \nabla \phi_i(\mathbf{r}) \cdot \nabla \phi_j(\mathbf{r}) \, d\mathbf{r} \\ &= \sum_{T_k \in \mathcal{T}} \sum_{k:\mathbf{V}_i, \mathbf{V}_j \in T_k} \sigma_k \int_{T_k} \nabla \phi_i(\mathbf{r}) \cdot \nabla \phi_j(\mathbf{r}) \, d\mathbf{r} \end{aligned}$$

where $\mathcal{T}$ represents the triangulation of Ω_h, and $\mathbf{V}_k$ the vertices of the tetrahedron T_k, and finally the right hand side of 11 is:

$$b_i = \int_{\Omega_h} \mathbf{J}_p \cdot \nabla \phi_i \, d\mathbf{r} = \int_{\Omega_h} \mathbf{q} \delta(\mathbf{r}_0) \cdot \nabla \phi_i \, d\mathbf{r} = \mathbf{q} \cdot \nabla \phi_i(\mathbf{r}_0)$$

3.3 The implicit Finite Element Method

3.3.1 iFEM for EEG

The implicit FEM works with the same formulation as the tFEM (10) but computes the integrals present in the stiffness matrix and the source term in a different manner. The integrals are evaluated on the voxels of the image, and so this method does not need any mesh generation and uses directly the grid provided by the MRI. In order to distinguish the different volumes that can have different conductivities, a level-set method is used to extract the surfaces from the MRI.
The computation of the stiffness matrix is then:

$$A_{i,j} = \sum_{k:\mathbf{P}_i \in V_k, \mathbf{P}_j \in V_k} \int_{V_k} \sigma(\mathbf{r}) \nabla \phi_k^i(\mathbf{r}) \cdot \nabla \phi_k^j(\mathbf{r})\, d\mathbf{r}$$

The Cartesian grid cannot match perfectly the geometry of the domains, and as domains can have different conductivities, we must split the integral in order to take into account each domains:

$$\int_{V_k} \sigma(\mathbf{r}) \nabla \phi_k^i(\mathbf{r}) \cdot \nabla \phi_k^j(\mathbf{r})\, d\mathbf{r} = \int_{V_k^1} \sigma_k^1 \nabla \phi_k^i(\mathbf{r}) \cdot \nabla \phi_k^j(\mathbf{r})\, d\mathbf{r} + \int_{V_k^2} \sigma_k^2 \nabla \phi_k^i(\mathbf{r}) \cdot \nabla \phi_k^j(\mathbf{r})\, d\mathbf{r}$$

Integration over a voxel crossing an interface is done thanks to the level-sets [9].

3.3.2 iFEM for MEG

A method for solving the forward problem in MEG has been developed by [11] using the adjoint approach. We refer to this article for further explanations.

3.4 Benefits and drawbacks of each methods

The symmetric BEM constructs a symmetric matrix, which is dense and can be stored; a direct solver is used to inverse it. The main drawback of this method is that it has to work on isotropic media with piecewise constant conductivities. On the other hand, we have the FEM:s that create huge but sparse matrices that cannot be inverted, the solution is obtained thanks to iterative solvers; here a preconditioned conjugated gradient. A significant advantage is that anisotropy and inhomogeneous media can be taken into account.

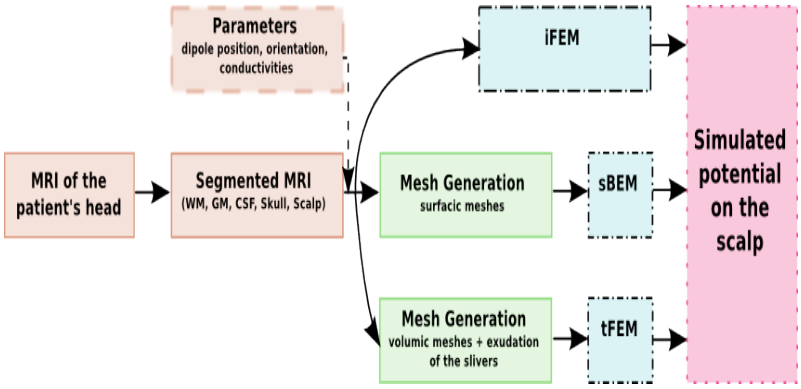

Figure 10: From the MRI acquisition to the simulated potential.

4 Quantitative comparisons of the results

In order to fairly compare the three methods, we have taken into account the precision of their results for a comparable amount of time/memory consumtion for the computations. Fig.10 shows the pipeline from an MRI acquisition to the result of the forward problem. We see the ease of use of the implicit FEM which bypasses the mesh generation. by simulating a dipole at 5 different locations on the Z-axis: {0.465, 0.615, 0.765, 0.8075, 0.8415} and oriented toward one of the following Cartesian direction: (1, 0, 1), (1, 1, 0), (0, 0, 1). Simulated potentials have been compared with the analytical ones.

4.1 The spherical model

The spherical model is widely used in the MEEG community, because it allows to get an analytical solution of the electric potential and the magnetic field. One can now use the analytic expression as a reference to compare the results coming from other methods. The analytic solution is given by [13] and [10]. The conductivities of the cortex and the scalp were set to 1 whereas the conductivity of the skull was set to 1/80. We computed the potential V in each x_i of the scalp mesh and measured two errors: the Relative Difference Measure (RDM) which is a topographical measure of the error and the Magnification error (MAG) which gives the amplitude of the errors. These errors are defined as:

$$RDM = \left\| \frac{V_{analytic}}{\|V_{analytic}\|} - \frac{V_{computed}}{\|V_{computed}\|} \right\| \qquad MAG = \frac{\|V_{computed}\|}{\|V_{analytic}\|} \tag{12}$$

$$\text{where} \quad \|V\| = \|V\|_2 = (\Sigma |V_i|^2)^{\frac{1}{2}}$$

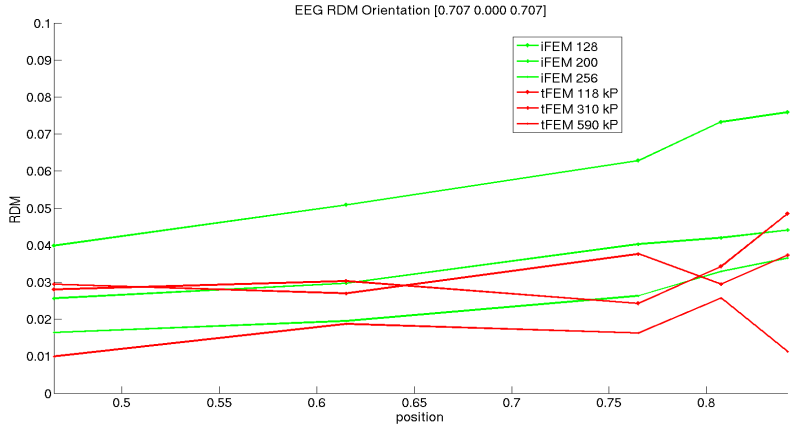

Figure 11: EEG — RDM with orientation [1 0 1].

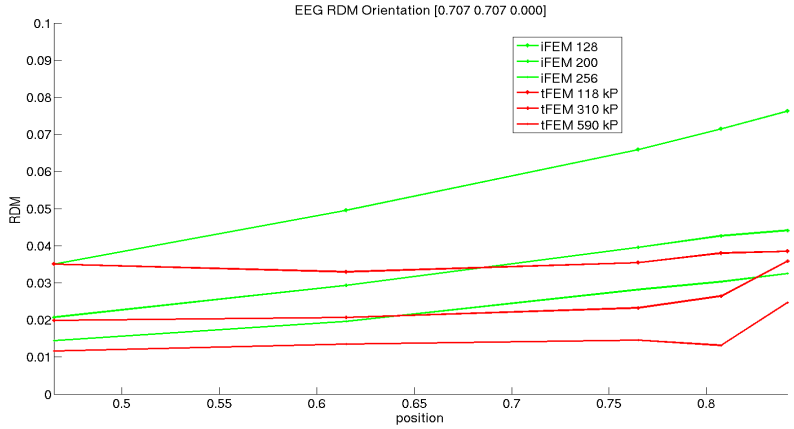

Figure 12: EEG — RDM with tangential orientation.

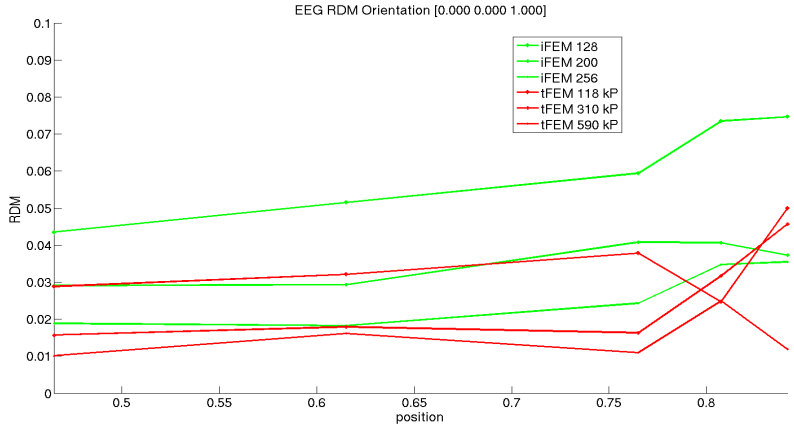

Figure 13: EEG — RDM with radial orientation.

4.2 Precisions of iFEM and tFEM

We have tested the precision of the two FE codes comparing them with the analytical solution. To do so, we have tested three meshes for the tFEM with: 118 000, 310 000, 590 000 points, and worked on images with dimensions: 128x128x128, 200x200x200, 256x256x256 for the iFEM.

Fig. 11 to 13 show a higher precision of the tFEM (in red) compared with the iFEM (in green) for the same amount of memory used. Computations made on the 590 000-points mesh has required 2.4 GB of RAM for the tFEM, and as well for the finest grid 256x256x256 used by the iFEM. Table.2 gives the times needed for computations. We have not yet solved an issue regarding the MAG of the iFEM, so it is not plotted; the MAG of the tFEM, will be shown in section 4.5. In exchange, one can see that results coming from the iFEM are more linear regarding the location of the dipoles for all orientations.

Methods	**NbPts — Dim**	**Assembling time**	**Iterations time**	**NbIterations**
tetrahedric	118 000	16 s	121 s	291
	310 000	45 s	702 s	416
	590 000	94 s	1852 s	509
implicit	128x128x128	82 s	338 s	337
	200x200x200	217 s	1728 s	509
	256x256x256	366 s	3824 s	579

Table 2: Computation time depending on the mesh size.

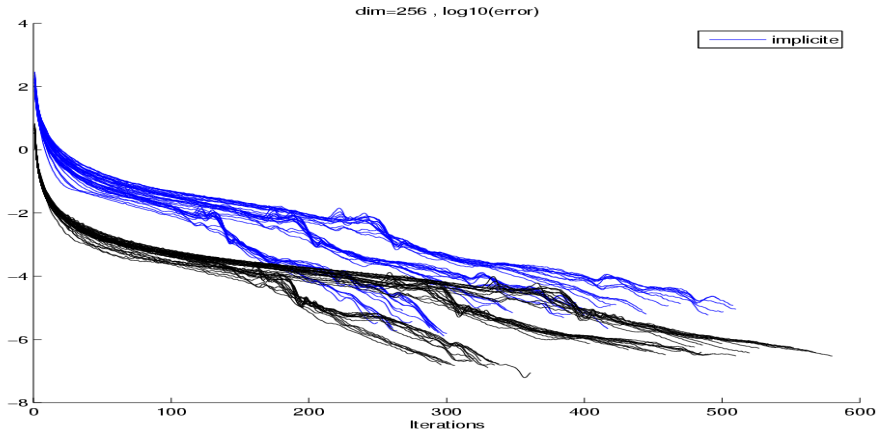

Figure 14: Decrease of the residuals through iterations: log(residue). Blue for the iFEM, and black for the tFEM.

Figure 14 presents the logarithm of the error through the iterative process for both codes. In blue, the implicit code for the three dimensions and all dipoles,

and in black the tetrahedral one. One can see a ratio between the errors of the iFEM and tFEM. In order to speed up computations one could also stop earlier.

4.3 Precision of the sBEM

The symmetric BEM developed in the software OpenMEEG[3], uses surfacic meshes. Several meshes have been generated with 228, 2 262, 6 121 , 7 289 total number of points. We first present the results for the EEG forward problem, and then the one of the MEG.

4.3.1 results for the EEG problem

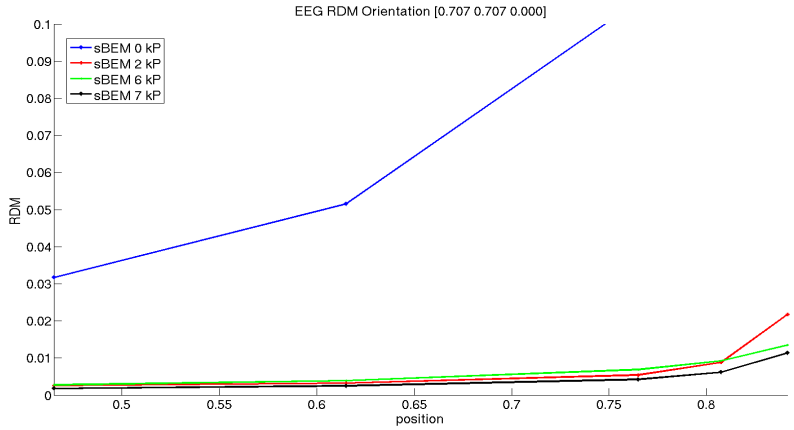

Figure 15: EEG — RDM with tangential orientation.

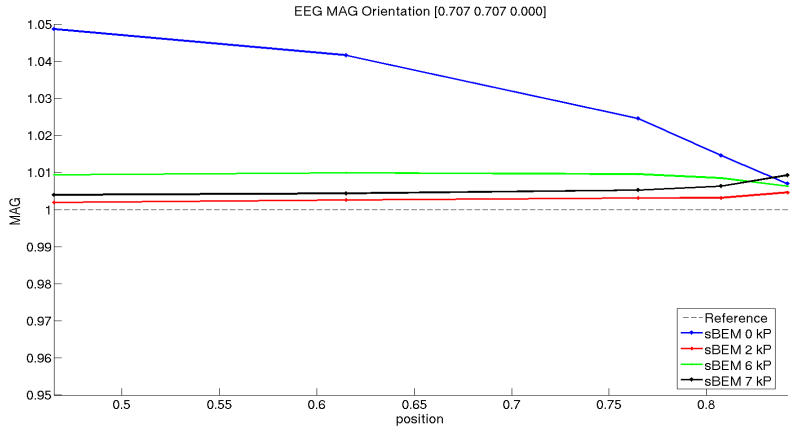

Figure 16: EEG — MAG with tangential orientation.

[3]http://openmeeg.gforge.inria.fr

Number of points	228	2 262	6 121	7 289
Computation Time	9 s	18 min	5 h 30	7 h

Table 3: Computation time depending on the mesh size.

The RDM is constantly below the 2% for all dipoles considering the meshes with 6 121 points and 7 289 points. Finally, table 3 gives the computation time[4] needed to solved a forward problem for all meshes. We see a high difference in time consumptions between the meshes of 2 262 and 6 121 points, whereas the error does not decrease significantly.

4.3.2 results for the MEG problem

Notice that the results shown in fig.17 and fig.18 do not share the same resolution on the y-axis than previous fig.15& 16. The errors are smaller than the ones of the EEG problem. Indeed, MEG is less sensitive to ohmic currents; the primary term in 2 dominates.

[4]Computations done on a 4 processors Xeon 3.20 GHz computer with 2 MB Cache and 8GB RAM

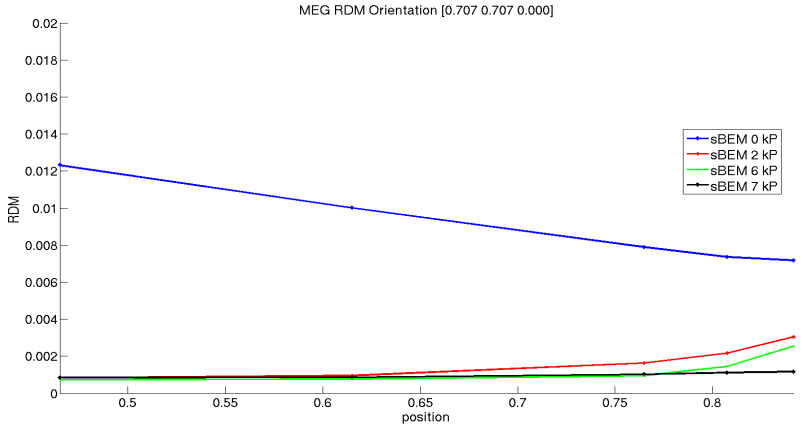

Figure 17: MEG — RDM with tangential orientation.

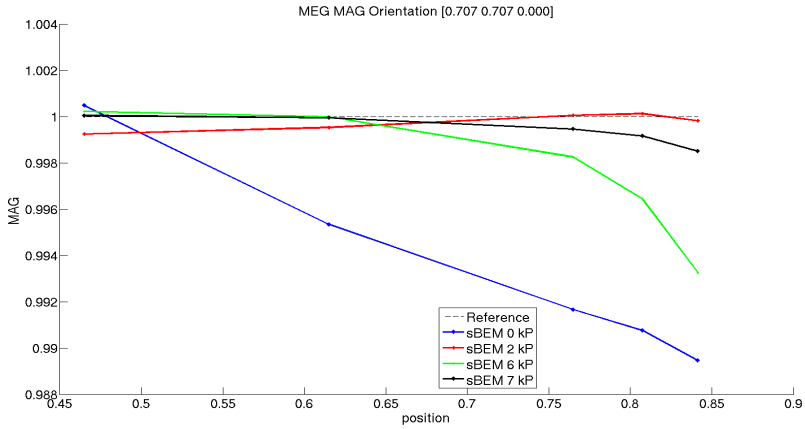

Figure 18: MEG — MAG with tangential orientation.

4.4 Realistic model and trials

On realistic models, analytical solution is not available, so one could test the precision by considering very high resolution model as a ground true and compare solutions with this model. We refer to [5].

4.5 Summary, for the spherical model, of all methods solving the forward EEG problem

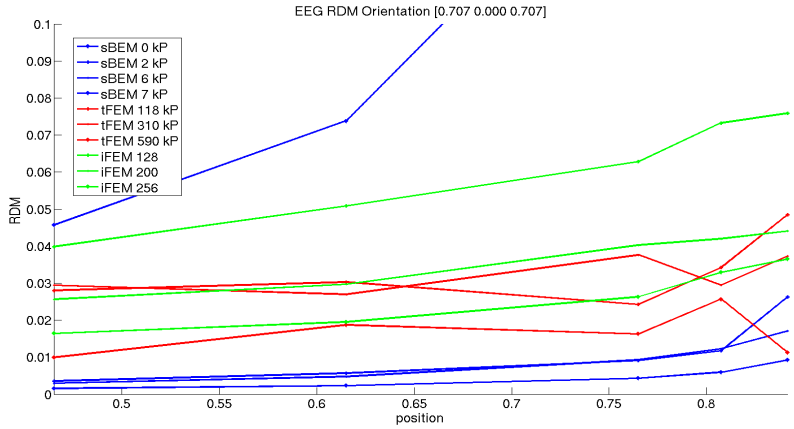

Figure 19: EEG — RDM of all methods.

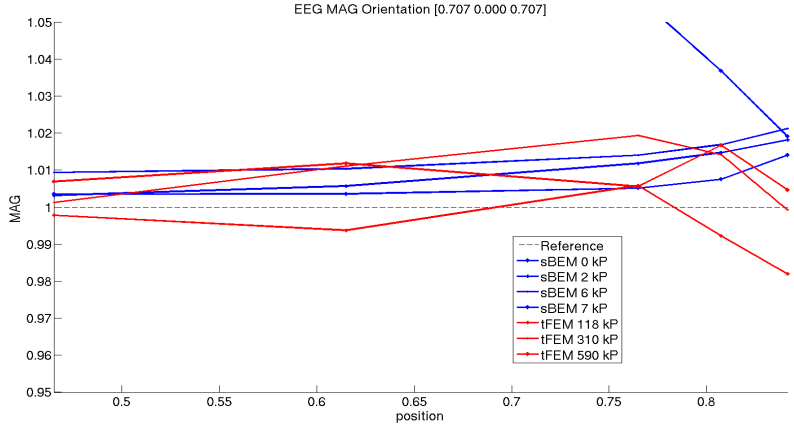

Figure 20: EEG — MAG of all methods.

On fig.19 and fig.20 are shown the errors for all methods.

5 Conclusion

In this document, we have seen how from a segmented MRI one could solve the MEEG forward problem. The sBEM gives the best results for the same amount of time spent in computations compared with the tetrahedric FEM, but the meshing step is still expensive. Furthermore, the sBEM is limited with the number of elements, and on realistic shape, it cannot provide a very detailed description of the geometry. Future computations on realistic model should clarify this point.
Even if the tFEM gives slightly better results, the iFEM remains easy to use and could be easy to parallelize.
The code Head_mesher could be optimized by reducing the time spent in the exudation of the slivers which in our case was responsible for 90% of the meshing time.
Finally, we recall that the sBEM cannot take into account anisotropy, such as the one of the skull.

References

[1] Marc Bonnet. *Equations intégrales et éléments de frontière*. CNRS Editions, Eyrolles, 1995.

[2] M. Clerc, G. Adde, J. Kybic, T. Papadopoulo, and J.-M. Badier. In vivo conductivity estimation with symmetric boundary elements. In Jaakko Malmivuo, editor, *International Journal of Bioelectromagnetism*, volume 7, pages 307–310, 2005.

[3] D. B. Geselowitz. On bioelectric potentials in an homogeneous volume conductor. *Biophysics Journal*, 7:1–11, 1967.

[4] J. Kybic, M. Clerc, T. Abboud, O. Faugeras, R. Keriven, and T. Papadopoulo. Integral formulations for the eeg problem. Technical Report 4735, INRIA, feb 2003.

[5] J. Kybic, M. Clerc, T. Abboud, O. Faugeras, R. Keriven, and T. Papadopoulo. A common formalism for the integral formulations of the forward EEG problem. *IEEE Transactions on Medical Imaging*, 24:12–28, jan 2005.

[6] J. Kybic, M. Clerc, O. Faugeras, R. Keriven, and T. Papadopoulo. Generalized head models for MEG/EEG: boundary element method beyond nested volumes. *Physics in Medicine and Biology*, 51:1333–1346, 2006.

[7] Gildas Marin, Christophe Guerin, Sylvain Baillet, Line Garnero, and Gérard Meunier. Influence of skull anisotropy for the forward and inverse problems in EEG: simulation studies using FEM on realistic head models. *Human Brain Mapping*, 6:250–269, 1998.

[8] Jean-Claude Nédélec. *Acoustic and Electromagnetic Equations*. Springer Verlag, 2001.

[9] Théodore Papadopoulo and Sylvain Vallaghé. Implicit meshing for finite element methods using levelsets. In *Proceedings of MMBIA 07*, 2007.

[10] Jukka Sarvas. Basic mathematical and electromagnetic concepts of the biomagnetic inverse problem. *Phys. Med. Biol.*, 32(1):11–22, 1987.

[11] S. Vallaghé, T. Papadopoulo, and M. Clerc. The adjoint method for general EEG and MEG sensor-based lead field equations. *Physics in Medicine and Biology*, 54:135–147, 2009.

[12] B. Yvert, O. Bertrand, J.-F. Echallier, and J. Pernier. Improved forward eeg calculations using local mesh refinement of realistic head geometries. *Electroencephalography and Clinical Neurophysiology*, 95:381–392, may 1995.

[13] Zhi Zhang. A fast method to compute surface potentials generated by dipoles within multilayer anisotropic spheres. *Phys. Med. Biol.*, 40:335–349, 1995.

Centre de recherche INRIA Sophia Antipolis – Méditerranée
2004, route des Lucioles - BP 93 - 06902 Sophia Antipolis Cedex (France)

Centre de recherche INRIA Futurs : Parc Orsay Université - ZAC des Vignes
4, rue Jacques Monod - 91893 ORSAY Cedex
Centre de recherche INRIA Nancy – Grand Est : LORIA, Technopôle de Nancy-Brabois - Campus scientifique
615, rue du Jardin Botanique - BP 101 - 54602 Villers-lès-Nancy Cedex
Centre de recherche INRIA Rennes – Bretagne Atlantique : IRISA, Campus universitaire de Beaulieu - 35042 Rennes Cedex
Centre de recherche INRIA Grenoble – Rhône-Alpes : 655, avenue de l'Europe - 38334 Montbonnot Saint-Ismier
Centre de recherche INRIA Paris – Rocquencourt : Domaine de Voluceau - Rocquencourt - BP 105 - 78153 Le Chesnay Cedex

Éditeur
INRIA - Domaine de Voluceau - Rocquencourt, BP 105 - 78153 Le Chesnay Cedex (France)
http://www.inria.fr
ISSN 0249-6399